

## Integrated Paramagnetic Resonance of High-Spin Co(II) in Axial Symmetry: Chemical Separation of Dipolar and Contact Electron–Nuclear Couplings

William K. Myers, Eileen N. Duesler, and David L. Tierney\*

Department of Chemistry and Chemical Biology, The University of New Mexico, Albuquerque, New Mexico 87131

Received February 7, 2008

Integrated paramagnetic resonance, utilizing electron paramagnetic resonance (EPR), NMR, and electron-nuclear double resonance (ENDOR), of a series of cobalt bis-trispyrazolylborates,  $\text{Co}(\text{Tp}^x)_2$ , are reported. Systematic substitutions at the ring carbons and on the apical boron provide a unique opportunity to separate through-bond and through-space contributions to the NMR hyperfine shifts for the parent, unsubstituted Tp complex. A simple relationship between the chemical shift difference ( $\delta_{\text{H}} - \delta_{\text{Me}}$ ) and the contact shift of the proton in that position is developed. This approach allows independent extraction of the isotropic hyperfine coupling,  $A_{\text{iso}}$ , for each proton in the molecule. The  $\text{Co} \cdot \cdot \text{H}$  contact coupling energies derived from the NMR, together with the known metrics of the compounds, were used to predict the ENDOR couplings at  $g_{\perp}$ . Proton ENDOR data is presented that shows good agreement with the NMR-derived model. ENDOR signals from all other magnetic nuclei in the complex ( $^{14}\text{N}$ , coordinating and noncoordinating,  $^{11}\text{B}$  and  $^{13}\text{C}$ ) are also reported.

### Introduction

The use of divalent cobalt as a spectroscopic surrogate for zinc is a well-established protocol in metallobiochemistry.<sup>1</sup> The cobalt ion typically adopts a high-spin (*hs*) configuration and a coordination geometry similar to that of the native zinc complex. In contrast to  $\text{Zn}(\text{II})$ , which is only accessible by X-ray absorption spectroscopy (XAS),<sup>2–9</sup> complexes of *hs*  $\text{Co}(\text{II})$ , including those of enzymes, are amenable to a wide array of spectroscopies, including

optical spectroscopy, XAS,<sup>10–17</sup> magnetic circular dichroism (MCD),<sup>18–24</sup> electron paramagnetic resonance

\* To whom correspondence should be addressed. E-mail: dtierney@unm.edu.

- (1) Maret, W.; Vallee, B. L. *Methods Enzymol.* **1993**, *226C*, 52–71.
- (2) Clark-Baldwin, K.; Tierney, D. L.; Govindaswamy, N.; Gruff, E. S.; Kim, C.; Berg, J.; Koch, S. A.; Penner-Hahn, J. E. *J. Am. Chem. Soc.* **1998**, *120*, 8401–8409.
- (3) Peariso, K.; Zhou, Z. H. S.; Smith, A. E.; Matthews, R. G.; Penner-Hahn, J. E. *Biochemistry* **2001**, *40*, 987–993.
- (4) Tobin, D. A.; Pickett, J. S.; Hartman, H. L.; Fierke, C. A.; Penner-Hahn, J. E. *J. Am. Chem. Soc.* **2003**, *125*, 9962–9969.
- (5) Okeley, N.; Paul, M.; Stasser, J.; Blackburn, N.; van der Donk, W. *Biochemistry* **2003**, *42*, 13613–13624.
- (6) Thomas, P. W.; Stone, E. M.; Costello, A. L.; Tierney, D. L.; Fast, W. *Biochemistry* **2005**, *44*, 7559–7565.
- (7) Costello, A. L.; Periyannan, G.; Yang, K.-W.; Crowder, M. W.; Tierney, D. L. *J. Biol. Inorg. Chem.* **2006**, *11*, 351–358.
- (8) Costello, A. L.; Sharma, N. P.; Yang, K.-W.; Crowder, M. W.; Tierney, D. L. *Biochemistry* **2006**, *45*, 13650–13658.
- (9) Reddi, A. R.; Guzman, T. R.; Breece, R. M.; Tierney, D. L.; Gibney, B. R. *J. Am. Chem. Soc.* **2007**, *129*, 12815–12827.

- (10) Zhang, K.; Chance, B.; Auld, D. S.; Larsen, K. S.; Vallee, B. L. *Biochemistry* **1992**, *31*, 1159–1168.
- (11) Lee, H. C.; Scheuring, E.; Peisach, J.; Chance, M. R. *J. Am. Chem. Soc.* **1997**, *119*, 12201–12209.
- (12) Buchko, G. W.; Hess, N. J.; Bandaru, V.; Wallace, S. S.; Kennedy, M. A. *Biochemistry* **2000**, *39*, 12441–12449.
- (13) deSeny, D.; Heinz, U.; Wommer, S.; Kiefer, M.; Meyer-Klaucke, W.; Galleni, M.; Frere, J. M.; Bauer, R.; Adolph, H. W. *J. Biol. Chem.* **2001**, *276*, 45065–45078.
- (14) Petros, A. K.; Shaner, S. E.; Costello, A. L.; Tierney, D. L.; Gibney, B. R. *Inorg. Chem.* **2004**, *43*, 4793–4795.
- (15) Breece, R. M.; Costello, A.; Bennett, B.; Sigdel, T. K.; Matthews, M. L.; Tierney, D. L.; Crowder, M. W. *J. Biol. Chem.* **2005**, *280*, 11074–11081.
- (16) Periyannan, G.; Costello, A. L.; Tierney, D. L.; Yang, K.-W.; Bennett, B.; Crowder, M. W. *Biochemistry* **2006**, *45*, 1313–1320.
- (17) Bresson, C.; Esnouf, S.; Lamouroux, C.; Solari, P. L.; Auwer, C. D. *New J. Chem.* **2006**, *30*, 416–424.
- (18) Coleman, J. E.; Coleman, R. V. *J. Biol. Chem.* **1972**, *247*, 4718–4728.
- (19) Nakata, M.; Ueyama, N.; Nakamura, A.; Nozawa, T.; Hatano, M. *Inorg. Chem.* **1983**, *22*, 3028–3035.
- (20) Bicknell, R.; Schaffer, A.; Waley, S. G.; Auld, D. S. *Biochemistry* **1986**, *25*, 7208–7215.
- (21) Werth, M. T.; Tang, S. F.; Formicka, G.; Zeppezauer, M.; Johnson, M. K. *Inorg. Chem.* **1995**, *34*, 218–228.
- (22) Larrabee, J. A.; Alessi, C. M.; Asiedu, E. T.; Cook, J. O.; Hoerning, K. R.; Klingler, L. J.; Okin, G. S.; Santee, S. G.; Volkert, T. L. *J. Am. Chem. Soc.* **1997**, *119*, 4182–4196.

(EPR),<sup>15,16,21,25–44</sup> NMR<sup>43–68</sup> and, more recently, electron–nuclear double resonance (ENDOR)<sup>69</sup> and high-frequency/

field EPR (HF/F-EPR).<sup>24,70,71</sup> While *hs* Co(II) typically delivers easily detectable features by all of these techniques, the interpretation of data is often limited to fingerprints, providing little structural detail. The presence of magnetic anisotropy, sizable spin–orbit couplings, and thermally accessible excited states hampers the analysis of spectroscopic observations in terms of structure and bonding. However, these same complications can serve to increase the information content of the data, provided they can be reliably assessed experimentally.

We report here the use of multifrequency EPR, ENDOR, and NMR to probe electron–nuclear couplings in a series of trigonal bis-trispyrazolylborate (Tp) chelates of *hs* cobalt(II). In addition to the structural analogy of pyrazole to imidazole,<sup>72</sup> the Tp chelates offer easy access to a number of structural homologues. Combined with the high symmetry of these systems, this allows for a more detailed analysis than is usually possible. In the following, we will develop the use of simple chemical substitutions to examine the relative contributions of contact and dipolar hyperfine coupling to the observed NMR hyperfine shifts. We then utilize the NMR-derived contact couplings, together with dipolar couplings calculated based on crystallographic distances and angles, to accurately simulate changes observed in ENDOR spectra for the same series of complexes. The limitations of this simple approach to determining the relative contributions of contact versus dipolar coupling for *hs* Co(II), potential refinements, and potential application to complexes of other first-row transition ions will also be discussed.

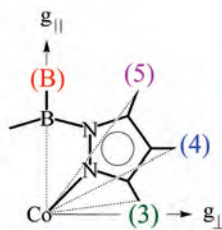
Following the convention of Trofimenko,<sup>73</sup> Co(Tp<sup>x</sup>)<sub>2</sub> refers to the symmetric bis-trispyrazolylborate cobalt(II) chelate, with pyrazole ring substituents indicated by the superscript “x”; substitutions at the boron atom are indicated in front of the Tp<sup>x</sup> designation. Members of the present series (Scheme 1) include the symmetric complexes, Co(Tp)<sub>2</sub>, Co(Tp<sup>3,5Me</sup>)<sub>2</sub>, Co(Tp<sup>3Me</sup>)<sub>2</sub>, Co(Tp<sup>4Me</sup>)<sub>2</sub>, and Co(*n*BuTp)<sub>2</sub>, as well as an asymmetric complex with a single pendant pyrazole, Co(TpQp), containing a Co ion coordinated by one trispyrazolylborate and one tetrapyrazolylborate. Magnetically, in

- (23) Larrabee, J. A.; Leung, C. H.; Moore, R. L.; Thamrong-Nawasawat, T.; Wessler, B. S. H. *J. Am. Chem. Soc.* **2004**, *126*, 12316–12324.
- (24) Krzystek, J.; Zvyagin, S. A.; Ozarowski, A.; Fiedler, A. T.; Brunold, T. C.; Telsler, J. *J. Am. Chem. Soc.* **2004**, *126*, 2148–2155.
- (25) Bencini, A.; Bertini, I.; Canti, G.; Gatteschi, D.; Luchinat, C. *J. Inorg. Biochem.* **1981**, *14*, 81–93.
- (26) Yim, M. B.; Kuo, L. C.; Makinen, M. W. *J. Magn. Reson.* **1982**, *46*, 247–256.
- (27) Benelli, C.; Bertini, I.; di Vaira, M.; Mani, F. *Inorg. Chem.* **1984**, *23*, 1422–1425.
- (28) Makinen, M. W.; Kuo, L. C.; Yim, M. B.; Wells, G. B.; Fukuyama, J. M.; Kim, J. E. *J. Am. Chem. Soc.* **1985**, *107*, 5245–5255.
- (29) Bicknell, R.; Hanson, G. R.; Holmquist, B.; Little, C. *Biochemistry* **1986**, *25*, 4219–4223.
- (30) Kang, P. C.; Eaton, G. R.; Eaton, S. S. *Inorg. Chem.* **1994**, *33*, 3660–3665.
- (31) Walsh, T. R.; Gamblin, S.; Emery, D. C.; MacGowan, A. P.; Bennett, P. M. *J. Antimicrob. Chemother.* **1996**, *37*, 423–431.
- (32) Bennett, B.; Holz, R. C. *J. Am. Chem. Soc.* **1997**, *119*, 1923–1933.
- (33) Walsh, T. R.; Neville, W. A.; Haran, M. H.; Tolson, D.; Payne, D. J.; Bateson, J. H.; MacGowan, A. P.; Bennett, P. M. *Antimicrob. Agents Chemother.* **1998**, *42*, 436–439.
- (34) Ustynyuk, L.; Bennett, B.; Edwards, T.; Holz, R. C. *Biochemistry* **1999**, *38*, 11433–11439.
- (35) D’Souza, V. M.; Bennett, B.; Copik, A. J.; Holz, R. C. *Biochemistry* **2000**, *39*, 3817–3826.
- (36) Shapir, N.; Osborne, J. P.; Johnson, G.; Sadowsky, M. J.; Wackett, L. P. *J. Bacteriol.* **2002**, *184*, 5376–5384.
- (37) Simm, A. M.; Higgins, C. S.; Carenbauer, A. L.; Crowder, M. W.; Bateson, J. H.; Bennett, P. M.; Clarke, A. R.; Halford, S. E.; Walsh, T. R. *J. Biol. Chem.* **2002**, *277*, 24744–24751.
- (38) Ozarowski, A.; Lee, H. M.; Balch, A. L. *J. Am. Chem. Soc.* **2003**, *125*, 12606–12614.
- (39) Crawford, P. A.; Yang, K. W.; Sharma, N.; Bennett, B.; Crowder, M. W. *Biochemistry* **2005**, *44*, 5168–5176.
- (40) Garrity, J. D.; Bennett, B.; Crowder, M. W. *Biochemistry* **2005**, *44*, 1078–1087.
- (41) Boyd, J. M.; Ensign, S. A. *Biochemistry* **2005**, *44*, 13151–13162.
- (42) Scarpellini, M.; Wu, A. J.; Kampf, J. W.; Pecoraro, V. L. *Inorg. Chem.* **2005**, *44*, 5001–5010.
- (43) Jacobsen, F. E.; Breece, R. M.; Myers, W. K.; Tierney, D. L.; Cohen, S. M. *Inorg. Chem.* **2006**, *45*, 7306–7315.
- (44) Tamayo, A.; Casabo, J.; Escriche, L.; Gonzalez, P.; Lodeiro, C.; Rizzi, A. C.; Brondino, C. D.; Passaggi, M. C. G.; Kivekaes, R.; Sillanpaae, R. *Inorg. Chem.* **2007**, *46*, 5665–5672.
- (45) LaMar, G. N.; Eaton, G. R.; Holm, R. H.; Walker, F. A. *J. Am. Chem. Soc.* **1973**, *95*, 63–75.
- (46) Bertini, I.; Lanini, G.; Luchinat, C. *J. Am. Chem. Soc.* **1983**, *105*, 5116–5118.
- (47) Luchinat, C.; Monnanni, R.; Sola, M. *Inorg. Chim. Acta* **1990**, *177*, 133–139.
- (48) Moratal, J. M.; Donaire, A.; Salgado, J.; Martinez-Ferrer, M. J. *J. Inorg. Biochem.* **1990**, *40*, 245–253.
- (49) Banci, L.; Dugad, L. B.; LaMar, G. N.; Keating, K. A.; Luchinat, C.; Pierattelli, R. *Biophys. J.* **1992**, *63*, 530–543.
- (50) Bertini, I.; Luchinat, C.; Pierattelli, R.; Vila, A. J. *Eur. J. Biochem.* **1992**, *208*, 607–615.
- (51) Bertini, I.; Luchinat, C.; Pierattelli, R.; Vila, A. J. *Inorg. Chem.* **1992**, *31*, 3975–3979.
- (52) Bencini, A.; Bertini, I.; Bini, T. *Inorg. Chem.* **1993**, *32*, 3312–3315.
- (53) Bertini, I.; Jonsson, B.-H.; Luchinat, C.; R.; Pierattelli, R.; Vila, A. J. *J. Magn. Reson. Ser. B* **1994**, *104*, 230–239.
- (54) Piccioli, M.; Luchinat, C.; Mizoguchi, T. J.; Ramirez, B. E.; Gray, H. B.; Richards, J. H. *Inorg. Chem.* **1995**, *34*, 737–742.
- (55) Salgado, J.; Jimenez, H. R.; Donaire, A.; Moratal, J. M. *Eur. J. Biochem.* **1995**, *231*, 358–369.
- (56) Salgado, J.; Jimenez, H. R.; Moratal, J. M.; Kroes, S.; Warmerdam, G. C. M.; Canters, G. W. *Biochemistry* **1996**, *35*, 1810–1819.
- (57) Briganti, F.; Pierattelli, R.; Scozzafava, A.; Supuran, C. T. *Eur. J. Med. Chem.* **1996**, *31*, 1001–1010.
- (58) Bertini, I.; Luchinat, C.; Mincione, G.; Pargi, G.; Gassner, G. T.; Ballou, D. P. *J. Biol. Inorg. Chem.* **1996**, *1*, 468–475.
- (59) Fernandez, C. O.; Sannazzaro, A. I.; Vila, A. J. *Biochemistry* **1997**, *36*, 10566–10570.
- (60) Donaire, A.; Salgado, J.; Moratal, J. M. *Biochemistry* **1998**, *37*, 8659–8673.
- (61) Tierney, D. L.; Gassner, G. T.; Luchinat, C.; Bertini, I.; Ballou, D. P.; Penner-Hahn, J. E. *Biochemistry* **1999**, *38*, 11051–11061.
- (62) Salgado, J.; Kalverda, A. P.; Diederix, R. E. M.; Canters, G. W.; Moratal, J. M.; Lawler, A. T.; Dennison, C. *J. Biol. Inorg. Chem.* **1999**, *4*, 457–467.
- (63) Diederix, R. E. M.; Canters, G. W.; Dennison, C. *Biochemistry* **2000**, *39*, 9551–9560.
- (64) Donaire, A.; Jimenez, B.; Moratal, J. M.; Hall, J. F.; Hasnain, S. S. *Biochemistry* **2001**, *40*, 837–846.
- (65) Harris, M. N.; Bertolucci, C. M.; Ming, L.-J. *Inorg. Chem.* **2002**, *41*, 5582–5588.
- (66) Fernandez, C. O.; Niizeki, T.; Kohzuma, T.; Vila, A. J. *J. Biol. Inorg. Chem.* **2003**, *8*, 75–82.
- (67) Dennison, C.; Sato, K. *Inorg. Chem.* **2004**, *43*, 1502–1510.
- (68) Knorr, R.; Hauer, H.; Weiss, A.; Polzer, H.; Ruf, F.; Loew, P.; Dvortsak, P.; Boehrer, P. *Inorg. Chem.* **2007**, *46*, 8379–8390.
- (69) Walsby, C. J.; Krepiy, D.; Petering, D. H.; Hoffman, B. M. *J. Am. Chem. Soc.* **2003**, *125*, 7502–7503.
- (70) Krzystek, J.; Zvyagin, S. A.; Ozarowski, A.; Trofimenko, S.; Telsler, J. *J. Magn. Reson.* **2006**, *178*, 174–183.
- (71) Lawrence, J.; Beedle, C. Y.; Yang, E.-C.; Ma, J.; Hill, S.; Hendrickson, D. N. *Polyhedron* **2007**, *26*, 2299–2303.
- (72) Bergquist, C.; Parkin, G. *J. Am. Chem. Soc.* **1999**, *121*, 6322–6323.
- (73) Trofimenko, S. *Scorpionates: The Coordination Chemistry of Pyrazolylborate Ligands*; Imperial College Press: London, 1999.

Scheme 1

	(3)	(4)	(5)	(B)
Tp	H	H	H	H
Tp <sup>3Me</sup>	CH <sub>3</sub>	H	H	H
Tp <sup>4Me</sup>	H	CH <sub>3</sub>	H	H
Tp <sup>3,5Me</sup>	CH <sub>3</sub>	H	CH <sub>3</sub>	H
<i>n</i> BuTp	H	H	H	<i>n</i> Bu
TpQp	H	H	H	(H, pz)*

\*one ligand has a B-H, while the other has a B-pz; pz = pyrazole.



both frozen and fluid solution, the six chelating pyrazolates appear symmetry equivalent, as do the two apical borons. Thus, for simplicity, as this report deals only with the cobalt chelates, we refer to each complex by reference to the ligand(s) alone. The structural variations being interrogated are color coded, as summarized in Scheme 1, throughout this report.

## Experimental Section

**Synthesis and Purification of Polypyrazolylborate Complexes.** All ligands were prepared according to published procedures.<sup>73</sup> Starting materials were obtained from commercial vendors and used without further purification. The metal complexes were prepared by reaction of solid CoCl<sub>2</sub>·6H<sub>2</sub>O with 2 equiv of the ligand, dissolved in a 50:50 (v/v) mixture of DMF and water. The resulting solution/suspension was extracted into toluene and separated by column chromatography on silica gel (19:1 toluene/methanol as eluent). Crystalline materials were obtained via slow evaporation of a toluene solution. The asymmetric compound, TpQp, was prepared in a similar fashion, by adding 1.1 equiv of CoCl<sub>2</sub> to a solution containing 1 equiv of each ligand. This procedure results in a distribution of products that is readily separable chromatographically.<sup>74</sup> Samples for spectroscopy were prepared directly from the crystalline material used for X-ray diffraction. All compounds were verified for mass and composition by high-resolution FAB-MS at the Nebraska Center for Mass Spectrometry (Univ. of Nebraska, Lincoln, NE).

**X-ray Structure Determinations.** Crystals were mounted on a standard Bruker X8 Apex2 CCD-based X-ray diffractometer equipped with an Oxford Cryostream 700 low temperature device and normal focus Mo-target X-ray tube ( $\lambda = 0.71073$  Å) operated at 1500 W (50 kV, 30 mA). X-ray intensities were measured at 233 K; the detector was placed at a distance 5.00 cm from the crystal. A full sphere of data consisting of 3111 frames was collected with a scan width of 0.5° in omega and phi with an exposure time of 10 s/frame. Frames were integrated with the Bruker SAINT software package using a narrow frame algorithm. Analysis of the data showed negligible decay during data collection; the data were processed with SADABS v. 2.10 and corrected for absorption. Structures were solved and refined with the Bruker SHELXTL v. 6.12 software package. All non-hydrogen atoms were refined anisotropically; hydrogen atoms on C were included and refined in ideal positions with isotropic  $U = 1.2U$  equiv. of the parent atom; H on B was included in the position seen in difference maps and its isotropic  $U$  was allowed to vary. Experimental details and crystallographic results for each structure are presented as Supporting Information.

**EPR Spectroscopy.** X- and Q-band (9 and 34 GHz, respectively) EPR spectra were acquired on a Bruker EMX EPR spectrometer,

with temperature maintained by either an Oxford ESR-900 (X-band) or an Oxford CF-935 (Q-band) liquid He cryostat. All EPR samples were prepared in a 50/50 toluene/dichloromethane glass at a concentration of 20 mM, except Tp<sup>4Me</sup>, which showed limited solubility (2 mM). Samples were degassed prior to EPR experiments by several cycles of freeze–pump–thaw. The power dependence of the X-band EPR signal was determined at several temperatures for each sample, with a minimum of 8 scans at each power setting, at each temperature (other conditions as noted above), at a minimum of six temperatures. Two independent temperature/power data sets were obtained for Co(Tp)<sub>2</sub> on samples obtained from different syntheses, giving identical results.

**NMR Spectroscopy.** NMR spectra were recorded on a Bruker ASX (300 MHz) spectrometer. Temperature control was accomplished with a liquid N<sub>2</sub> evaporator and the heater/thermocouple provided with the instrument. Chemical shifts were referenced to the <sup>1</sup>H resonances of the solvent, toluene. All NMR samples were 20 mM in toluene-*d*<sub>8</sub> (except as noted above for Tp<sup>4Me</sup>, 2 mM), and all were subjected to several freeze–pump–thaw cycles prior to data collection. Spectra obtained in 50/50 toluene-*d*<sub>8</sub>/CD<sub>2</sub>Cl<sub>2</sub> were indistinguishable from those obtained in neat toluene-*d*<sub>8</sub>. The spectra, presented in Figure 4 and Supporting Information, Figure S8, are the average of 256 scans (1024 for Tp<sup>4Me</sup>) that consist of 8k data points over a spectral window of 150 kHz (500 ppm), using a 3 μs excitation pulse. Prior to Fourier transformation, the FID was smoothed by exponential multiplication, which incorporated an additional line width of 5 Hz.

**ENDOR Spectroscopy.** Continuous wave (CW) X-band ENDOR spectra were recorded at the National Biomedical EPR Center at the Medical College of Wisconsin (Milwaukee, WI) on a Bruker Elexsys EPR spectrometer equipped with a Bruker ENDOR accessory. The spectra in Figure 5 and Supporting Information, Figure S7, were obtained from thoroughly degassed samples of 5 mM Co(Tp<sup>3</sup>)<sub>2</sub> in 50/50 *d*<sub>8</sub>-toluene/CD<sub>2</sub>Cl<sub>2</sub> and represent the average of 128 scans each, with 25 kHz frequency-modulation (100 kHz depth) of the rf (18 W) using 20 mW of microwave power to saturate the EPR signal; all other conditions were as used for the EPR studies. The low intensity of the EPR signal at  $g_{||}$  precluded the collection of ENDOR data at fields that ranged far from  $g_{\perp}$ .

## Results

X-ray diffraction<sup>75</sup> and X-band, single-crystal EPR<sup>76</sup> of the parent compound, Tp, were first reported in the late 1960s. Proton NMR spectra at 60 MHz were later reported and discussed for Tp, Tp<sup>3,5Me</sup>, and *n*BuTp.<sup>77–81</sup> Optical studies, combined with the single-crystal EPR results, established the  $g$ -tensor orientation, with  $g_{||}$  along the molecular 3-fold, and suggested that the <sup>4</sup>E orbital doublet lay lowest in energy,<sup>76</sup> although the <sup>4</sup>A<sub>2</sub> orbital singlet is

(74) A second structural isomer of TpQp was isolated from this reaction. It appears to contain a five-coordinate Co(II), formed from a tridentate Tp ligand and a bidentate Qp. Fractions of the two parent compounds, CoTp<sub>2</sub> and CoQp<sub>2</sub>, were also obtained. The Qp<sub>2</sub> and five-coordinate TpQp compounds are not fully characterized.

(75) Churchill, M. R.; Gold, K.; Maw, C. E., Jr. *Inorg. Chem.* **1970**, *9*, 1597–1604.

(76) Jesson, J. P. *J. Chem. Phys.* **1966**, *45*, 1049–1056.

(77) Jesson, J. P. *J. Chem. Phys.* **1967**, *47*, 579–581.

(78) Jesson, J. P. *J. Chem. Phys.* **1967**, *47*, 582–591.

(79) Jesson, J. P.; Trofimenko, S.; Eaton, D. R. *J. Am. Chem. Soc.* **1967**, *89*, 3148–3158.

(80) McGarvey, B. R. *J. Chem. Phys.* **1970**, *53*, 86–91.

(81) LaMar, G. N.; Jesson, J. P.; Meakin, P. *J. Am. Chem. Soc.* **1971**, *93*, 1286–1288.



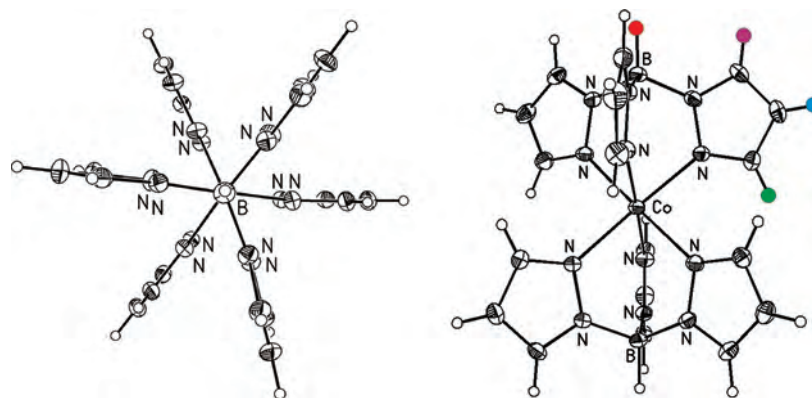


**Figure 1.** X-ray structure of  $\text{Co}(\text{Tp})_2$ , axial (left) and equatorial (right) views. The colored spheres represent the symmetry distinct sets of protons in the molecule, following the color scheme described in Scheme 1, and followed throughout.

**Table 1.** Metal–Nitrogen and Metal–Proton Metrics for  $\text{Co}(\text{Tp}^x)_2$  and  $\text{Co}(\text{TpQp})$

complex	$\text{Co}\cdots\text{N}^a$	$\text{Co}\cdots\text{BH}^a$	$\text{Co}\cdots\text{5H}^a$	$\text{Co}\cdots\text{4H}^a$	$\text{Co}\cdots\text{3H}^a$	$r_{\text{N}-\text{N}}^b$ (intra)	$r_{\text{N}-\text{N}}^b$ (inter)	N–Co–N <sup>c</sup> bite angle
$\text{Co}(\text{Tp})_2$	2.124 (52°)	4.35 (0°)	5.04 (33°)	5.21 (61°)	3.44 (84°)	2.89	3.13	85.5°
$\text{Co}(\text{Tp}^{4\text{Me}})_2$	2.124 (52°)	4.25 (0°)	5.01 (31°)	6.16 (62°)	3.45 (86°)	2.88	3.12	84.5°
$\text{Co}(\text{Tp}^{3\text{Me}})_2$	2.162 (52°)	4.33 (0°)	5.03 (32°)	5.26 (60°)	3.73 (92°)	2.96	3.15	86.4°
$\text{Co}(\text{Tp}^{3,5\text{Me}})_2$	2.138 (52°)	4.29 (0°)	5.87 (29°)	5.21 (61°)	3.69 (93°)	2.93	3.11	86.8°
$\text{Co}(n\text{BuTp})_2$	2.116 (51°)	5.25 (7°) <sup>c</sup>	5.04 (32°)	5.23 (61°)	3.33 (86°)	2.87	3.12	84.9°
$\text{Co}(\text{TpQp})$	Tp	2.128 (52°)	$\beta\text{CH}_2$ (5.9)	$\gamma\text{CH}_2$ (7.3)	$\delta\text{CH}_3$ (8.7)	2.87	3.12	86.0°
	Qp		5.02 (33°)	5.20 (61°)	3.42 (85°)			
	pz		5.02 (33°)	5.16 (61°)	3.38 (86°)			
			7.61 (13°)	7.57 (10°)	5.54 (22°)			84.9°

<sup>a</sup> Average distances in Å, with  $\theta$  (defined as  $\text{B}\cdots\text{Co}\cdots\text{n}$ ) in parentheses. <sup>b</sup> Average intraligand and interligand N⋅N distances in Å. <sup>c</sup> Distances and angles for the protons of the *n*-butyl group's  $\alpha\text{CH}_2$ . <sup>d</sup> Average of 6 N–Co–N bite angles; three each for  $\text{Co}(\text{TpQp})$ .

predicted.<sup>82</sup> Since that time, this class of symmetric cobalt chelates has received surprisingly little attention. The  $\text{Tp}^{3\text{Me}}$ ,  $\text{Tp}^{4\text{Me}}$ , and  $\text{TpQp}$  complexes are reported here for the first time.

**Comparison of the Solid-State Structures.** X-ray structures were determined for all six compounds. Each shows a  $\text{Co}^{2+}$  ion held in a pseudo-octahedral local environment ( $\text{CoN}_6$ ), with the global symmetry of the molecule ( $D_{3d}$ , except  $\text{TpQp}$ ,  $C_{3v}$ ) determined by the 3-fold axis defined by the  $\text{B}\cdots\text{Co}\cdots\text{B}$  vector (Figure 1, Scheme 1). Selected distances and angles relevant to the paramagnetic resonance studies described below are listed in Table 1.

Comparison of the intra- and interligand N⋅N (donor) distances,  $r_{\text{N}-\text{N}}$  in Table 1, indicates a significant axial elongation along the  $\text{B}\cdots\text{Co}\cdots\text{B}$  ( $C_3$ ) axis, with  $\sim 2.9$  Å between coordinating nitrogens of the same  $\text{Tp}^x$  ligand, versus  $\sim 3.1$  Å between nitrogens on opposite  $\text{Tp}^x$  ligands. The Co–N bond lengths are uniform ( $\pm 0.008$  Å) within each compound, with the exception of  $\text{Tp}^{4\text{Me}}$ , which shows a small (0.028 Å) tetragonal elongation along opposite Co–N bonds (this leads to a slightly shorter  $\text{Co}\cdots\text{BH}$  distance relative to Tp in the solid state, Table 1). Solution NMR and EPR studies (below) show that this distortion is averaged in solution. The two complexes with methyl groups in the 3-position ( $\text{Tp}^{3\text{Me}}$  and  $\text{Tp}^{3,5\text{Me}}$ ) show slightly longer Co–N distances (by  $\sim 0.038$  and 0.012 Å, respectively), and this results in a slightly larger bite angle ( $\sim 1$ – $2^\circ$ , Table 1). However, only the  $\text{Tp}^{3\text{Me}}$  complex shows an outward expansion normal to the  $C_3$  axis ( $r_{\text{N}-\text{N}}$  inter, Table 1). Interestingly, this leads to a slight compression along the

$\text{B}\cdots\text{Co}\cdots\text{B}$  axis, indicated by a decrease in the  $\text{Co}\cdots\text{BH}$  distance of 0.02 Å. The 5-methyls in  $\text{Tp}^{3,5\text{Me}}$  compress the ligand further along the  $C_3$  (Table 1), and this is reflected in a still shorter  $\text{Co}\cdots\text{BH}$  distance (0.06 Å shorter than in Tp).

Spatial adjustment of the ligand to accommodate substitutions affects minimal variation in the metal–proton metrics ( $r$ ,  $\theta$  in Table 1). All metal–proton distances across the series are  $\pm 0.05$  Å, with  $\theta \pm 3^\circ$  (relative to  $\text{B}\cdots\text{Co}\cdots\text{B}$ ). The methyl proton distances in Table 1 were obtained by a rotational average about the  $\text{C}_{\text{pyrazole}}-\text{C}_{\text{methyl}}$  bond, defining a point  $\sim 0.3$ , 0.9, and 0.8 Å further from the  $\text{Co}^{2+}$  ion for 3-, 4-, and 5-Me groups, respectively, relative to 3-, 4-, and 5-H in Tp. Perhaps more importantly for the present study, the average methyl proton position subtends a similar angle  $\theta$ , aside from an  $8^\circ$  increase for the 3-methyl of  $\text{Tp}^{3\text{Me}}$ <sup>83</sup> and  $7^\circ$  for the  $\alpha\text{CH}_2$  of *n*BuTp.

**EPR Spectroscopy.** The high symmetry of the series of  $\text{Tp}^x$  chelates is reflected in the axial symmetry of their EPR spectra ( $g_{\parallel}^{\text{eff}} \approx 8$  and  $g_{\perp}^{\text{eff}} \approx 1$ , Figure 2A, lines colored according to Scheme 1). A summary of the experimentally observed EPR parameters is given in Table 2. The feature at  $g = 2$  is a predicted parallel transition,<sup>84</sup> although the reasons for its presence or absence, for a particular complex, are unclear. Well-resolved  $^{59}\text{Co}$  hyperfine is observed at  $g_{\parallel}^{\text{eff}}$  (Figure 2B), and the magnitudes of both  $A_{\parallel}^{\text{obs}}$  (92–94 G) and  $g_{\parallel}^{\text{eff}}$  (8.45–8.50) are fairly insensitive to peripheral substitutions, with the exception of  $\text{Tp}^{3\text{Me}}$  (89 G and 8.34). Together with the axial symmetry of the spectra, this implies

(83) The  $\pi/2$ -symmetry of  $\theta$  in an axial system renders this only a  $4^\circ$  differential.

(84) Weltner, W., Jr. *Magnetic Atoms and Molecules*; Dover Publications: Mineola, NY, 1983.

(82) Orgel, L. E. *J. Chem. Phys.* **1955**, *23*, 1004–1014.

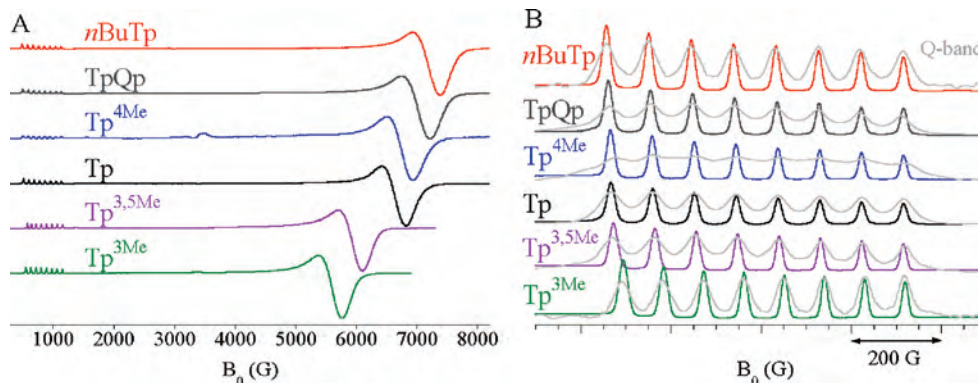


**Figure 2.** (A) X-band EPR spectra of Co(Tp)<sub>2</sub> and Co(TpQp) (colored lines, as labeled). (B) Expanded view of the  $g_{11}$  region, comparing X-band (same colors as in (A)) and Q-band spectra (gray lines, offset horizontally for comparison). Conditions:  $T = 3.6$  K;  $\nu_{MW} = 9.4$  GHz (0.2 mW) or 33.8 GHz (0.1 mW); 5 G field modulation (100 kHz); receiver gain = 5000; time constant = 82 ms.

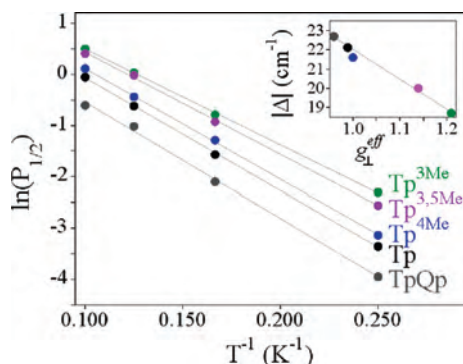


**Figure 3.** Temperature dependence of power at half-saturation ( $P_{1/2}$ ) of the  $g_{\perp}$  transition for Co(Tp)<sub>2</sub> and its derivatives at X-band. Inset: Correlation between the position of  $g_{\perp}$  (each point can be identified by color, as in (A)) and the EPR-derived value of  $|\Delta|$ .

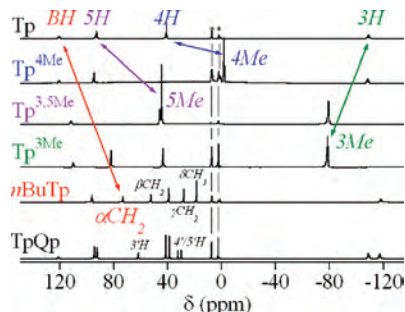


**Figure 4.** 300 MHz <sup>1</sup>H NMR of Co(Tp)<sub>2</sub> and its derivatives. Signals from residual toluene are marked with asterisks and indicated by vertical lines; other assignments as labeled. The colored arrows follow the color palette in Scheme 1 and represent the change in chemical shift that accompanies a given methyl substitution, as discussed in the text.

that  $g_{11}$  in frozen solution is coincident with the molecular 3-fold axis, as was indicated by the single crystal studies of Tp.<sup>76</sup> The apparent  $m_l$ -dependence of the intensity and width of successive hyperfine lines can be indicative of the presence of  $g$ -strain, with further support provided by comparison of the parallel transition at X- and Q-band (Figure 2B).<sup>85–87</sup> For each complex, the hyperfine line width increases 3- to 6-fold from X- to Q-band. The Tp<sup>4Me</sup> complex, which

displays a small tetragonal distortion in the solid state (above), shows the largest line width increase. Only small variations in bite angle are seen throughout the series of complexes (84.5–86.8°, Table 1), and no clear correlation between bite angle and  $g_{\perp}^{\text{eff}}$  is apparent.

The “in-plane”  $g_{\perp}^{\text{eff}}$  transition is more intimately linked to the conformation of the complex. For example, 3-methyl substitution leads to expansion of the ligand in the perpendicular plane (Table 1), and Tp<sup>3Me</sup> shows the largest  $g_{\perp}^{\text{eff}}$  of the series (1.26). The intraligand N••N distance in the disubstituted Tp<sup>3,5Me</sup> complex is intermediate to that of Tp and Tp<sup>3Me</sup>, and this chelate displays a  $g_{\perp}^{\text{eff}}$  (1.18) that is intermediate to Tp and Tp<sup>3Me</sup>. The 4-methyl substitution has the least steric considerations of any of the substituted complexes, and its  $g_{\perp}^{\text{eff}}$  of 1.00 is nearly identical to Tp. Substitutions on boron, as in TpQp and *n*BuTp, lead to a reduction in  $g_{\perp}^{\text{eff}}$ , 0.97 and 0.94 respectively, also consistent with  $g_{11}$  along B••Co••B in frozen solution. Some correlations can be drawn between bite angle and  $g_{\perp}^{\text{eff}}$ . For example, complexes with 3-methyl substituents displayed the largest average bite angles and the largest  $g_{\perp}^{\text{eff}}$ ; complexes with bulky substituents on boron showed the smallest average bite angles and the smallest values of  $g_{\perp}^{\text{eff}}$ .

Power-saturation studies demonstrate that the power at half-saturation,  $P_{1/2}$ , can be directly correlated with the position of  $g_{\perp}^{\text{eff}}$ . At every temperature investigated,  $P_{1/2}$  increases throughout the series (3Me > 3,5Me > 4Me ~ Tp > TpQp; the temperature/power dependence for *n*BuTp was not measured). Although the correlation of EPR saturation behavior and  $|\Delta|$  for *hs* Co(II)<sup>26,28</sup> is far less reliable than values obtained by MCD<sup>22,24</sup> or HF/F-EPR,<sup>24,70</sup> the relative comparison presented here (Figure 3, Table 2) shows a clear trend within the series of compounds. The data indicate that the EPR-derived “ $|\Delta|$ ”, which more likely reports on EPR (electron) relaxation than large scale electronic structure, increases in the same order as above, tracking with the position of  $g_{\perp}^{\text{eff}}$ . The 4 K spectra are consistent with an effective  $M_S = \pm 1/2$  ground state, in accord with Jesson’s original model.<sup>76</sup>

**NMR Spectroscopy.** Consistent with the expected symmetry equivalence of the six chelating pyrazole rings and the two apical boron atoms, the symmetric Tp<sup>x</sup><sub>2</sub> complexes

(85) Froncisz, W.; Scholes, C. P.; Hyde, J. S.; Wei, Y.-H.; King, T. E.; Shaw, R. W.; Beinert, H. *J. Biol. Chem.* **1979**, *254*, 7482–7484.

(86) Froncisz, W.; Hyde, J. S. *J. Chem. Phys.* **1980**, *73*, 3123–3131.

(87) Mabbs, F. E.; Collison, D. *Electron Paramagnetic Resonance of d Transition Metal Compounds*; Elsevier: Amsterdam, 1992.

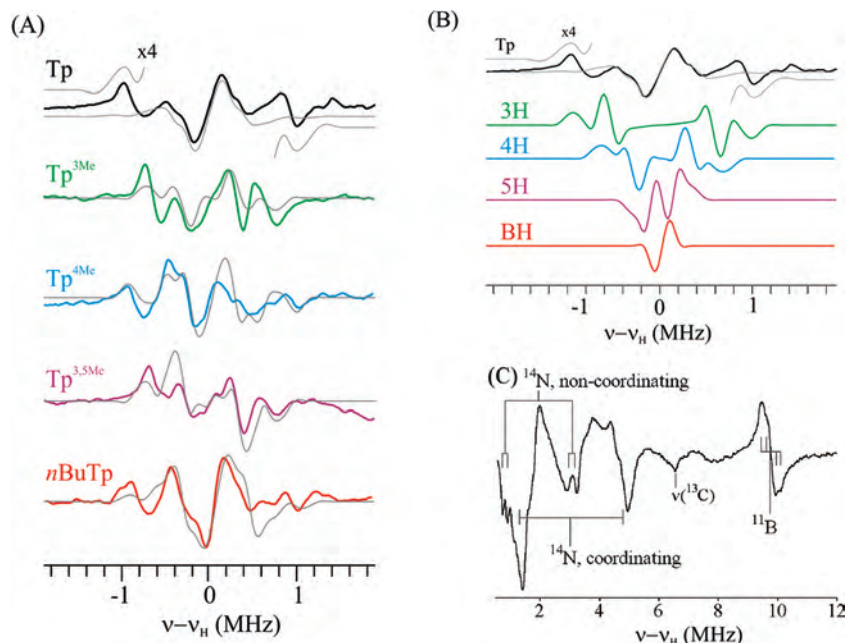


**Figure 5.** X-band CW ENDOR of  $\text{Co}(\text{Tp}^x)_2$ . (A) Proton region at  $g_{\perp}$ , centered at  $\nu_H$ . For each experimental spectrum (colored lines, as labeled), a simulation based on the NMR-derived couplings, as described in the text, is presented as an overlay (gray lines). (B) Individual proton contributions to the total simulation for  $\text{Co}(\text{Tp})_2$  in part A, following the color palette of Scheme 1. (C) Low-frequency region at  $g_{\perp}$  for  $\text{Co}(\text{Tp})_2$ . The brackets are included to guide the discussion of the spectra given in the text.

**Table 2.** EPR Parameters for Octahedral  $\text{Co}(\text{Tp}^x)_2$  and  $\text{Co}(\text{TpQp})^a$

	Q-band		X-band	
	$g_{\parallel}$ ( $A_{\parallel}$ , $\Delta\nu_{1/2}$ ) <sup>b</sup>	$g_{\perp}$ ( $A_{\perp}$ , $\Delta\nu_{1/2}$ )	$g_{\parallel}$ ( $A_{\parallel}$ , $\Delta\nu_{1/2}$ )	$g_{\perp}$ ( $\Delta\nu_{1/2}$ )
$\text{Co}(n\text{BuTp})_2$	8.50 (94, 61)	8.50 (94, 22)	0.94 (1300)	24
$\text{Co}(\text{TpQp})$	8.49 (93, 81)	8.49 (93, 22)	0.97 (1300)	23
$\text{Co}(\text{Tp})_2$	8.48 (93, 77)	8.48 (93, 21)	1.02 (1400)	21
$\text{Co}(\text{Tp}^{4\text{Me}})_2$	8.47 (93, 127)	8.47 (93, 20)	1.00 (1600)	21
$\text{Co}(\text{Tp}^{3,5\text{Me}})_2$	8.45 (92, 70)	8.45 (92, 21)	1.18 (1100)	19
$\text{Co}(\text{Tp}^{3\text{Me}})_2$	8.34 (89, 53)	8.34 (89, 20)	1.26 (1600)	17

<sup>a</sup> All spectra were collected at  $T = 3.6$  K with 5 G field modulation (100 kHz), time constant = 82 ms, 0.2 mW (X-band, 9.38 GHz) or 0.1 mW (Q-band, 33.8 GHz) microwave power, receiver gain =  $5 \times 10^3$  at 9.38 and 33.8 GHz. <sup>b</sup> Values of  $A_{\parallel}$  reported in gauss; fwhm ( $g_{\parallel}$ ) or baseline-to-baseline line width ( $g_{\perp}$ ) in gauss. <sup>c</sup> Values in  $\text{cm}^{-1}$ , based on a fit to the temperature dependence of  $P_{1/2}$ .<sup>26,28</sup> The value of  $|\Delta|$  given for  $n\text{BuTp}$  (italic) is an estimate, based on the inset to Figure 3.

show simple four-line  $^1\text{H}$  NMR spectra (Figure 4). The overall pattern of  $^1\text{H}$  chemical shifts for Tp is suggestive of substantial dipolar coupling, with one negative (3H,  $\theta \approx 90^\circ$ ,  $3 \cos^2 \theta - 1 \approx -1$ ) and three increasingly positive shifts (4H < 5H < BH, decreasing  $\theta$ ). The pattern of chemical shifts establishes that the room temperature, fluid solution orientation of  $g_{\parallel}$  is also along  $\text{B} \cdots \text{Co} \cdots \text{B}$ , as it is in frozen solution, based on the EPR (above). Any other arrangement would require only positive dipolar shifts be observed. For example, taking the N–Co–N direction as  $g_{\parallel}$ ,  $\theta$  (3H, 4H, 5H) =  $10^\circ$ ,  $19^\circ$ , and  $33^\circ$ ; none of these angles is greater than  $57^\circ$ ; this orientation cannot account for the presence of a large, negative chemical shift.

The reduced symmetry of the TpQp complex results in a 10 line NMR spectrum. It is composed of a single BH resonance, three pairs corresponding to the 3-, 4-, and 5-protons of inequivalent Tp and Qp ligands, and three lines from the 3'-, 4'-, and 5'-protons of the noncoordinating ("dangling") pyrazole. The inequivalent pairs are not symmetrically disposed about the chemical shift of the unsub-

**Table 3.** NMR Assignments for  $\text{Co}(\text{Tp}^x)_2$  at 297 K<sup>a</sup>

	BH	5H	4H	3H	R
$\text{Co}(n\text{BuTp})_2$		97	39	-118	74 ( $\alpha\text{CH}_2$ ) 53 ( $\beta\text{CH}_2$ ) 28 ( $\gamma\text{CH}_2$ ) 19 ( $\delta\text{CH}_3$ )
$\text{Co}(\text{TpQp})$	Qp	94	39	-117	62 (3'H) 33, 30 (4'H, 5'H)
	Tp	121	92	-109	
$\text{Co}(\text{Tp})_2$		121	93	-109	
$\text{Co}(\text{Tp}^{4\text{Me}})_2$		121	95	-2	-108
$\text{Co}(\text{Tp}^{3,5\text{Me}})_2$		112	44	46	-79
$\text{Co}(\text{Tp}^{3\text{Me}})_2$		110	82	44	-78

<sup>a</sup> Chemical shifts in ppm, referenced to the resonances of residual toluene.

stituted Tp complex. For each pair,  $3\text{H}^{\text{Tp}}/3\text{H}^{\text{Qp}}$  (ca. -110 ppm),  $4\text{H}^{\text{Tp}}/4\text{H}^{\text{Qp}}$  (ca. 40 ppm) and  $5\text{H}^{\text{Tp}}/5\text{H}^{\text{Qp}}$  (ca. 94 ppm), one resonance falls very near the chemical shift of the parent Tp complex, and the other, presumably from the Qp ligand, is shifted away from this position. Using this as the basis for assignment (Table 3), the observed pattern,  $\Delta\delta' = (\delta_{\text{Tp}} - \delta_{\text{Qp}}) = -8.7$  (3H),  $-2.8$  (4H),  $+2.5$  (5H), suggests that the protons of the coordinating pyrazoles of the Qp ligand experience a slightly different, perhaps competing dipolar field relative to the corresponding protons of the Tp ligand, although no added rhombicity is apparent in the EPR. The protons of the dangling pyrazole, which are also expected to carry little or no through-bond coupling, exhibit substantial dipolar hyperfine shifts for protons at distances greater than 7.5 Å from the Co ion. This is also true for the  $n\text{BuTp}$  complex, where the  $\delta\text{CH}_3$  protons, nearly 9 Å from the metal ion, are shifted to 19 ppm.

#### Separation of Contact and Dipolar Hyperfine Shifts.

The differences noted above in the solid-state structures translate into only minor perturbations in the room temperature NMR spectra. For example, the 4H proton resonances range from 41–46 ppm across the entire set of compounds, further supporting the conclusion that the various methyl substitutions have minimal effect on the electronic structure



of the Co ion. We were interested in using the methyl (alkyl) substitutions at various positions to gain insight into the relative levels of contact and dipolar coupling between the Co ion and the protons of the parent compound, Tp. In his pioneering work in this area, Jesson attempted to use the hyperfine shift of the terminal methyl of the *n*-butyl group in *n*BuTp to estimate the relative contributions of dipolar and contact coupling.<sup>77,78</sup> The *n*BuTp  $\delta_{\text{CH}_3}$  dipolar shift was used to predict the dipolar contribution to the hyperfine shifts of the ring protons for several complexes, by the ratio of their relative distances.<sup>88</sup> However, in all cases, including the parent Tp complex, Jesson's predicted hyperfine shifts differed from the observed shifts by as much as 50%. It should be noted that at the time of Jesson's work, no X-ray data was available, for *any* of the complexes. The theory was subsequently refined by McGarvey to include the contribution of low-lying excited states and second order Zeeman effects,<sup>80</sup> correctly predicting non-Curie temperature dependence and total shifts closer to the experimental values.<sup>81</sup>

Our goal was not to theoretically evaluate or predict, but rather to experimentally, empirically isolate the relative contributions of contact and dipolar coupling mechanisms to the observed hyperfine shifts. The ratio method employed previously by Jesson<sup>78</sup> necessarily proffers correlated results, as each proton's coupling is determined relative to a reference proton's coupling. We chose to generate the methyl(alkyl)-substituted derivatives to facilitate the development of a difference method, which decouples the analysis of one position on the molecule from all others, allowing for direct and independent assessment of the spin delocalization at every proton position. Extending Jesson's initial condition,<sup>78</sup> we assume that *all* methyl and butyl proton hyperfine shifts are purely dipolar in origin. This is equivalent to assuming that the pyrazolylborates are exclusively  $\sigma$ -donors, in accord with previous studies of scorpionate complexes.<sup>22,89,90</sup> For the purpose of the present analysis, substitution at the apical boron was modeled with the  $\alpha\text{CH}_2$  of *n*BuTp. There is no evidence, based on the NMR, for hindered rotation about the B–C(CH<sub>2</sub>) bond in *n*BuTp (Figure 4), validating use of the  $\alpha\text{CH}_2$  in the analysis that follows.

In the limit of complete attenuation of contact coupling for an alkyl substituent, the difference in chemical shift between corresponding methyl and proton resonances must approximately equal the contact shift exhibited by the proton in that position. Decreased dipolar coupling to the more distant methyl protons leads to an additional, predictable attenuation of the hyperfine shift, dependent on the ratio of the metal–proton distances,  $(R_{\text{H}}/R_{\text{Me}})^3$ . Within these limits, the Tp proton contact shift,  $\delta_{\text{H}}^{\text{C}}$ , can be defined algebraically in terms of the observed chemical shift difference,  $\Delta\delta^{\text{obs}}$  ( $\delta_{\text{H}} - \delta_{\text{Me}}$ ). Equation 1 expresses  $\delta_{\text{H}}^{\text{C}}$  in terms of the Tp proton

**Table 4.** Contact and Dipolar Contributions to the Hyperfine Shifts of  $\text{Co}(\text{Tp})_2^a$

	$\delta^{\text{obs}}$	$\delta^{\text{dia}}$	$\delta_{\text{H}}^{\text{P}}$	$\delta_{\text{H}}^{\text{Cb}}$	$\delta_{\text{H}}^{\text{D}}$	$A_{\text{iso}}^{\text{c}}$	$\Delta\delta^{\text{obs}}$	$(R_{\text{H}}/R_{\text{Me}})^3$
BH	121	5	116	32	84	1.27	47	0.82
5H	93	6	87	27	60	1.07	49	0.63
4H	41	5	36	49	–13	1.94	43	0.61
3H	–109	6	–115	–7	–108	–0.27	–31	0.78

<sup>a</sup> Symbols as defined in the text. Reference shifts,  $\delta^{\text{dia}}$ , are for the sodium salt of the ligand in 50/50 D<sub>2</sub>O/*d*-DMF. <sup>b</sup> From eq 1. <sup>c</sup> Indirectly, from eq 2B (adjusted, see text).

hyperfine shift ( $\delta_{\text{H}}^{\text{C}}$ ), the chemical shift difference ( $\Delta\delta^{\text{obs}}$ , above), and the ratio of the metal–proton distances ( $R_{\text{H}}$  and  $R_{\text{Me}}$ , Table 1). All of the terms on the right side of eq 1 are experimentally determined (Table 4). A full development of eq 1 is included as Supporting Information; the resulting values of  $\delta_{\text{H}}^{\text{C}}$  from this analysis are summarized in Table 4. Extraction of the contact shift gives, by difference, the dipolar contribution, as well. Modification of eq 1, allowing for a small amount of contact coupling to the methyl protons, predicts accordingly larger contact couplings for a given proton (see Supporting Information, eq S10).

$$\delta_{\text{H}}^{\text{C}} = \frac{\Delta\delta^{\text{obs}} - \delta_{\text{H}}^{\text{P}} \left( 1 - \left( \frac{R_{\text{H}}}{R_{\text{Me}}} \right)^3 \right)}{\left( \frac{R_{\text{H}}}{R_{\text{Me}}} \right)^3} \quad (1)$$

This approach is analogous to the ratio method developed by Horrocks and co-workers,<sup>91,92</sup> which relies on the ratio of hyperfine shifts for Ni<sup>2+</sup> (purely dipolar) and Co<sup>2+</sup> (contact + dipolar) homologues. The ratio method is limited in application to complexes where a similar geometry and electronic structure is adopted by two different metal ions, with dramatically different coordination preferences. In contrast, selective ligand substitutions can potentially separate the paramagnetic shift into its components directly, for any synthetically accessible ligand system, and complexes of many Kramer's ions. By examining complexes of the same metal, in the same geometry and environment, each position that is substituted can be probed, *independent of all other positions on the molecule*. By establishing a high degree of electronic similarity, more detailed analyses can offer deeper insight into systems with more complex electronic structure, such as *hs* Co(II). Only small, systematic variations are apparent in the crystallography, the EPR, and the NMR of the present series. The structural and electronic perturbations across the set result in less than 2% changes in metal–proton distances/angles. One more subtle advantage of selective substitution is that the sign of the isotropic coupling is implicit in the frequency shift that accompanies a given substitution (Table 4).

**Use of the NMR Contact Shifts To Predict the ENDOR Spectra.** Both NMR and ENDOR measure the hyperfine interaction between unpaired electrons and nearby nuclei. These energies are manifest in both the NMR chemical shift

(88) McConnell, H. M.; Robertson, R. E. *J. Chem. Phys.* **1958**, *29*, 1361–1365.

(89) Inscore, F. E.; McNaughton, R.; Westcott, B. L.; Helton, M. E.; Jones, R.; Dhawan, I. K.; Enemark, J. H.; Kirk, M. L. *Inorg. Chem.* **1999**, *38*, 1401–1410.

(90) Desrochers, P. J.; Telsler, J.; Zvyagin, S. A.; Ozarowski, A.; Krzystek, J.; Vivic, D. A. *Inorg. Chem.* **2006**, *45*, 8930–8941.

(91) Horrocks, W. deW., Jr.; Taylor, R. C.; LaMar, G. N. *J. Am. Chem. Soc.* **1964**, *86*, 3031–3038.

(92) Kluiber, R. W.; Horrocks, W. deW., Jr. *J. Am. Chem. Soc.* **1965**, *87*, 5350–5356.

and in the ENDOR splittings. Therefore, the ENDOR couplings can be used to test the accuracy of the NMR-derived isotropic couplings. The ENDOR couplings are also a sum of dipolar and contact coupling energies, to first order,  $A_{\text{obs}} = A_{\text{iso}} + T$ , where  $A_{\text{iso}}$  is the isotropic (contact) coupling and  $T$  is the tensor form of the dipolar coupling, which takes the form  $T = [-T, -T, 2T]$ , with  $T$  given by eq 2A. When  $g$  is highly anisotropic, the observed dipolar hyperfine couplings are scaled by the ratio of the observing  $g$ -value and the free-electron value,  $A_{\text{obs}} = A_{\text{iso}} + (g_{\text{obs}}/g_e)T$ .<sup>93</sup>

$$T = \frac{g_N \beta_N \times g_e \beta_e}{r^3} (3 \cos^2 \theta - 1) \quad (2A)$$

$$\delta^c = \frac{A_{\text{iso}} g_{\text{av}} \mu_B S(S+1)}{2\pi 3\gamma kT} \quad (2B)$$

Given prior knowledge of the structure of the complex, and the orientation of the  $g$ -tensor within the molecular frame, the dipolar contribution to the ENDOR couplings can be calculated accurately for high-spin systems such as these,<sup>94–96</sup> without reference to the NMR chemical shift. In the absence of significant second-order effects, the NMR contact shifts can be directly related to the isotropic couplings,  $A_{\text{iso}}$ , according to eq 2B.<sup>97</sup> McGarvey has shown that use of eq 2B with  $S = 3/2$  for these trigonal chelates underestimates the true value of  $A_{\text{iso}}$  for a given contact shift by approximately 50%, because of significant second-order Zeeman effects (see eq 53 in ref 80).<sup>80</sup> As is discussed below, this correction improves the quality of the ENDOR simulations, and it is the corrected values that are reported in Table 4.

**ENDOR Spectroscopy.** Continuous wave X-band <sup>1</sup>H ENDOR of CoTp<sub>2</sub> at  $g_{\perp}$  agrees with the analysis of the NMR data. For ligand atoms at  $g_{\perp}$ , to first order,  $A_{\text{obs}} \approx A_{\text{iso}} - (g_{\perp}/g_e)T$ . The <sup>1</sup>H ENDOR spectra for the series are presented in Figure 5A (colored lines, as indicated in the figure and summarized in Scheme 1). The ENDOR spectra also make the case for the frozen solution  $g$ -tensor orientation being aligned with the B••Co••B direction, as it is in fluid solution. Placement of  $g_{\parallel}$  along one pair of Co–N bonds necessarily requires that two symmetry distinct sets of pyrazoles be observed, in turn requiring the presence of seven distinct <sup>1</sup>H ENDOR signals, or at a minimum, much more poorly resolved spectra than those observed.

To test the accuracy of the isotropic couplings derived from the NMR data, the ENDOR spectra were simulated with the program DIPSIM,<sup>94,95,98,99</sup> which calculates the ENDOR spectrum from a user input value of  $A_{\text{iso}}$  and a

calculated value for  $T$ , defined by user input values for the internuclear distance ( $r$ ) and the polar angles  $\theta$  and  $\phi$ .<sup>100</sup> Use of eq 2B ( $g_{\text{av}} = 3.17$ ) to obtain  $A_{\text{iso}}$  does slightly underestimate the observed ENDOR splittings, and adjusting the result of eq 2B by a factor of 1.5, according to McGarvey's relationship,<sup>80</sup> improves the already good agreement with the experimental spectra. The adjusted values of  $A_{\text{iso}}$  are reported in Table 4.

The total simulations, shown as gray lines in Figure 5A, are the sum of the expected contributions from the four symmetry-distinct types of protons in each molecule, calculated utilizing either the NMR-derived value of  $A_{\text{iso}}$  for a given proton (Table 4), or  $A_{\text{iso}} = 0$  for the corresponding methyl group, and the crystallographically determined values of  $r$  and  $\theta$  (Table 1), and finally scaled to their degeneracies (six for each pyrazolate proton, two for the boron-bound species). As can be seen from the simulations, the predicted ENDOR patterns agree well with experiment. The simulations deviate from the observed splittings, in most cases, by less than 5%, suggesting the isotropic coupling to the methyl protons is indeed minimal. Individual contributions for the parent complex are presented in Figure 5B. Scaled summation of these contributions gives the total simulation presented in Figure 5A. A similar process was followed to generate all of the simulations in Figure 5A. Comparison of the parent complex with the various derivatives shows the predictable gain and loss of signals anticipated for a given substitution (Supporting Information, Figure S6).

In addition to the constitutive protons, ENDOR signals are readily detected for all other types of magnetic nuclei in the complex. The low-frequency region of the X-band ENDOR spectrum for Tp at  $g_{\perp}$  (Figure 5C) shows well-resolved signals from both types of nitrogen (coordinating and noncoordinating). The two <sup>14</sup>N patterns in Figure 5C demonstrate the two limiting cases for ENDOR patterns. The larger coupling (presumed to arise from the coordinating nitrogens) is centered at half the hyperfine coupling,  $A/2$ , and split by twice the Larmor frequency (the <sup>14</sup>N quadrupole couplings are not resolved), while the smaller coupling (from the noncoordinating nitrogens) is centered at the <sup>14</sup>N Larmor frequency, and split by the hyperfine coupling,  $A$ . Also apparent in Figure 5C is a poorly resolved <sup>11</sup>B ( $I = 3/2$ ) quartet from the symmetry equivalent, apical boron atoms, and a small signal at the <sup>13</sup>C Larmor frequency, possibly from natural abundance <sup>13</sup>C. Similar patterns are observed for the entire series (Supporting Information, Figure S7).

## Discussion

**Integration of NMR, EPR, and ENDOR.** The present studies highlight several benefits of integrating nuclear and electron paramagnetic resonance. For example, NMR provides access to ligand atoms at considerable distances (e.g., the terminal methyl protons of *n*BuTp at greater than 9 Å from the Co ion) but is unable to probe nearest neighbor

(93) Hutchison, C. A.; McKay, D. B. *J. Chem. Phys.* **1977**, *66*, 3311–3330.

(94) Tierney, D. L.; Huang, H.; Martasek, P.; Masters, B. S. S.; Silverman, R. B.; Hoffman, B. M. *Biochemistry* **1999**, *38*, 3704–3710.

(95) Tierney, D. L.; Huang, H.; Martasek, P.; Roman, L. J.; Silverman, R. B.; Hoffman, B. M. *J. Am. Chem. Soc.* **2000**, *122*, 7869–7875.

(96) Tierney, D. L.; Huang, H.; Martasek, P.; Roman, L. J.; Silverman, R. B.; Masters, B. S. S.; Hoffman, B. M. *J. Am. Chem. Soc.* **2000**, *122*, 5405–5406.

(97) Bertini, I.; Luchinat, C. *NMR of Paramagnetic Substances*; Elsevier: Amsterdam, 1996.

(98) Tierney, D. L.; Rocklin, A. M.; Lipscomb, J. D.; Que, L., Jr.; Hoffman, B. M. *J. Am. Chem. Soc.* **2005**, *127*, 7005–7013.

(99) The program DIPSIM is available from Dr. Peter Doan, Northwestern University, upon request.

(100) The angle  $\phi$  is undefined in axial symmetry.



atoms. ENDOR provides relatively easy access to intimately coupled nuclei, such as the coordinating and noncoordinating nitrogens and the apical borons, in addition to direct confirmation of the NMR-derived  $^1\text{H}$  coupling energies. The proton magnetic resonance provides an excellent example of an area where nuclear and electron paramagnetic resonance methods directly overlap. The boron nuclei present another example where the two techniques directly overlap, as  $^{11}\text{B}$  NMR chemical shifts have been reported for Tp and  $n\text{BuTp}$ .<sup>78</sup>

The present studies also demonstrate that the use of selective substitution can provide direct access to the relative magnitudes of through-bond and through-space electron–nuclear couplings via the change in hyperfine shifts. Substitution of a methyl group in place of a proton is often synthetically accessible, making this approach reasonably general for small molecule studies. The current studies have further shown that the  $^1\text{H}$  ENDOR patterns can be reasonably reproduced, using these NMR-derived parameters. At its current level, the NMR analysis adequately estimates the ENDOR couplings, while largely neglecting the influence of the physical state of the samples (frozen vs fluid solution) employed in the two experiments, and potentially non-negligible isotropic couplings to the methyl protons (although negative isotropic couplings would be required for the 4Me, 5Me and  $n\text{Bu}$   $\alpha\text{CH}_2$  protons in order to improve the agreement with the ENDOR). However, the methodology developed here, in the absence of significant structural perturbations, is empirical and adjustable (see Supporting Information, eq S10), allowing for refinement in the result as measurements improve.

For the present series, the presence of unquenched orbital momentum in the Co(II) ion's ground-state provides a further complication. The accuracy of  $A_{\text{iso}}$  derived from a fluid solution, NMR-observable ( $\Delta\delta$ ), and its subsequent use to predict the frozen solution ENDOR, depends on the model used to convert  $\delta_{\text{H}}^{\text{eff}}$ . Near the limit of complete attenuation of contact coupling on substitution,  $\delta_{\text{H}}^{\text{eff}}$  remains a model-independent observable. The simplest model (eq 2A and 2B), assuming isotropic Fermi contact couplings, with traceless dipolar tensors that conform to the point-dipole approximation, reasonably reproduced the observed ENDOR patterns at  $g_{\perp}^{\text{eff}}$ , and it did so for all of the chemical substitutions examined. Applying an algebraic correction, based on a model that includes spin–orbit and second-order effects,<sup>80</sup> improved the agreement in all cases.

The known presence of large spin–orbit interactions is expected to lead to contact couplings ( $A_{\text{iso}}$ ) that are not isotropic, and dipolar coupling tensors ( $T$ ) that are not traceless.<sup>101,102</sup> Further, the preceding analysis unnecessarily assumes that all six Kramer's doublets display an identical  $A_{\text{iso}}$ , which, if incorrect, can lead to large discrepancies between the ground-state interaction measured by ENDOR at low temperature and the thermal average interaction observed by NMR at room temperature. The influence of

spin–orbit and second-order effects on couplings within the ground-state should be apparent in the relative size and asymmetry of  $A_{\perp}$  versus  $A_{\parallel}$ ,<sup>77,80</sup> and a more detailed assessment requires, at a minimum, ENDOR studies, such as those presented in Figure 5 and Supporting Information, Figure S7, at  $g_{\perp}^{\text{eff}} \approx 8$ . Any potential variation in  $A_{\text{iso}}$  for different, thermally accessible doublets is likely to only be observable in a detailed, temperature-dependent NMR study.

In effect, the current report represents a comparison of only one data point from each regime, ENDOR at only one field position and NMR at only one temperature, and its extension in either dimension would dramatically increase the information content of the data. While the use of EPR and ENDOR is generally limited to Kramer's ions, the chemical substitution and NMR methodology described here can, in principle, be applied to complexes of any NMR-accessible transition metal ion, Kramer's or non-Kramer's. The simple model employed in this “single-point” comparison, between the fluid solution NMR and the frozen solution ENDOR, should be generally applicable, especially in the absence of an orbital contribution to the metal ion's ground state.

**Spin Densities.** The spectra in Figure 5 and Supporting Information, Figure S7, mark only the second report of ENDOR signals from ligand atoms coupled to a  $hs$  Co(II) center.<sup>69</sup> Bearing in mind the preceding caveats, the ability to observe ENDOR signals from all but the ring carbons affords the opportunity for a cursory assessment of the extent of delocalization in the complex. The effects of unquenched orbital momentum on the hyperfine couplings, as discussed above, are particularly important to the analysis of hyperfine coupling to the  $^{59}\text{Co}$  nucleus. For more distant atoms, the observed hyperfine couplings are up to 2 orders of magnitude smaller (the largest  $^1\text{H}$  coupling observed at  $g_{\perp}^{\text{eff}}$  is only ca. 2 MHz). Thus, regardless of the mechanism by which they arise, the spin densities on the ligand nuclei are small.

At  $g_{\perp}^{\text{eff}}$ , the dipolar coupling to the coordinated nitrogens is expected to be  $<0.3$  MHz, suggesting that the 6 MHz coupling exhibited at  $g_{\perp}^{\text{eff}}$  by the coordinated  $^{14}\text{N}$  can be considered almost entirely isotropic in origin (intrinsic  $a_{\perp} \approx 6$  MHz).  $A_{\text{iso}}$  can be related to the spin density on each atom, according to eq 3, where  $\rho_{\text{N}}$  is the spin density,  $A_0$  is the hyperfine coupling expected for a full electron residing in the atomic orbital in question, and  $S$  is the total spin of the complex.

$$A_{\text{iso}} = \rho_{\text{N}} \frac{A_0}{2S} \quad (3)$$

Using  $A_0(^{14}\text{N}) = 1809 \text{ MHz}^{103}$  in eq 3,  $A_{\text{iso}}(^{14}\text{N}) = 6 \text{ MHz}$  corresponds to  $\sim 1\%$  total N  $2s$  spin density, per coordinated nitrogen (or 6% total for 6 equivalent  $^{14}\text{N}$ ). While this does not consider any anisotropic component, such contributions are expected to be small. Similarly, the noncoordinating  $^{14}\text{N}$  couplings correspond to an intrinsic isotropic hyperfine of  $\sim 2 \text{ MHz}$ , or 0.3% each (2% of the total spin density). The apical boron nuclei present only a poorly resolved quartet

(101) Thornley, J. H. M.; Windsor, C. G.; Owen, J. *Proc. Roy. Soc. (London)* **1965**, *284*, 252–271.

(102) Abragam, A.; Bleaney, B. *Electron Paramagnetic Resonance of Transition Ions*; 2nd ed.; Clarendon Press: Oxford, 1970.

(103) Weil, J. A.; Bolton, J. R.; Wertz, J. E. *Electron Paramagnetic Resonance*; Wiley: New York, 1994.

at  $g_{\perp}$ , suggesting that  $A_{\text{iso}}$  is approximately  $-1/2 T$  (ca. 0.13 MHz), corresponding to 0.15% total  $2s$  spin density per boron nucleus ( $A_0(^{11}\text{B}) = 255 \text{ MHz}$ ).<sup>103</sup> The protons, with  $A_0(^1\text{H}) = 1420 \text{ MHz}$ ,<sup>103</sup> account for another 4% ( $3\text{H} \sim 0.3$ ,  $4\text{H} \sim 2.0$ ,  $5\text{H} \sim 1.2$ , and  $\text{BH} \sim 0.5\%$ ). In all, the observed ligand atom couplings at  $g_{\perp}^{\text{eff}}$  account for  $\sim 12\%$  of the total spin, supporting the assertion that the trispyrazolylborates are primarily  $\sigma$ -donor ligands, with little  $\pi$ -interaction with the central metal ion. This is consistent with recent electronic structural studies of Tp complexes with Co, as well as with other metals.<sup>22,89,90</sup>

**Fluxional Motion.** The small tetragonal distortion noted in the  $\text{Tp}^{4\text{Me}}$  structure likely belies a small dynamic process in solution, based on the symmetry equivalence of all six pyrazoles, in every complex, in all methods employed. The  $\text{Tp}^{4\text{Me}}$  compound elongates along one of the N–Co–N directions by  $0.028 \text{ \AA}$  ( $\Delta r$ ) in the solid state (no other complex in the series shows more than a  $0.008 \text{ \AA}$  distortion in the solid state,  $\Delta r/R_{\text{avg}} < 0.1\%$ ). Compared to the  $2.14 \text{ \AA}$  average Co–N bond lengths ( $\Delta r/R_{\text{avg}} = 1.4\%$ ) and the average  $0.24 \text{ \AA}$  trigonal elongation ( $\Delta r/R_{\text{N–N}} = 12\%$ ), the tetragonal contribution should be considered only a minor perturbation on the electronic structure of the system, which is dominated by trigonal symmetry. Motion on such a small-scale is, however, likely to “smear” (or strain) the apparent  $g$ -tensor.

The agreement of the  $^1\text{H}$  NMR and ENDOR patterns indicates that any such process is equally active in fluid and frozen solution, suggesting that large-scale electronic rearrangement does not occur. The NMR spectra do not show significant line broadening over a wide range of temperatures (Supporting Information, Figure S8), indicating that any fluxional process would have to occur faster than the NMR time scale ( $\sim 10^9 \text{ s}^{-1}$ ), to temperatures below  $227 \text{ K}$ . We believe the best description of this system in solution is one in which the magnetic  $z$ -axis,  $\text{B} \bullet \bullet \text{Co} \bullet \bullet \text{B}$ , wobbles along three degenerate, tetragonal directions, giving the appearance of a slight precession of the  $g$ -tensor about the  $z$ -axis. Motion on this time scale is likely to have minimal effect on the observed metal–proton hyperfine couplings displayed in the NMR, in which such a process will be rotationally averaged

for a small molecule, and in the EPR and ENDOR, in which this uncertainty would be orientationally averaged and probably absorbed in the EPR line width. The similarity of the EPR, NMR, and ENDOR spectra, across the series, requires they all adopt similar conformations in solution. This leads to the conclusion that all members of the present series likely undergo some level of dynamic distortion of this kind in solution, and that it must, therefore, be averaged on the NMR time scale. As we will show in a subsequent submission, the effect of this motion on the NMR relaxation behavior of these complexes in solution is remarkable.

**Acknowledgment.** The authors wish to acknowledge thorough and instructive review in the preparation of this manuscript. We would also like to thank Dr. Karen Ann Smith for tireless technical assistance; Ms. Meita Fulton, Mr. Mikel Roberts, and Dr. Dorothy Miller for their assistance in the preliminary experiments; Dr. Brian Bennett for his assistance in the acquisition of the X-band ENDOR spectra and many helpful discussions; and Dr. Peter E. Doan for his software, his generosity, and his expertise. This work was supported by the National Science Foundation (CHE-0518189 to D.L.T.). The X-/Q-band EPR spectrometer (CHE-0216277) and X-ray diffractometer (CHE-0443580) were purchased with funds provided by the National Science Foundation. The National Biomedical EPR Center at the Medical College of Wisconsin is supported by the National Institutes of Health (NIH P41 EB001980).

**Supporting Information Available:** ORTEPs for  $\text{Co}(\text{Tp}^{3\text{Me}})_2$  (Figure S1),  $\text{Co}(\text{Tp}^{3,5\text{Me}})_2$  (Figure S2),  $\text{Co}(\text{Tp}^{4\text{Me}})_2$  (Figure S3),  $\text{Co}(\text{TpQp})$  (Figure S4), and  $\text{Co}(n\text{BuTp})_2$  (Figure S5) are included. Structural information is also available in CIF format. A stack plot comparing the  $^1\text{H}$  ENDOR for  $\text{Co}(\text{Tp}^x)_2$  to the  $^1\text{H}$  ENDOR of the parent complex,  $\text{Co}(\text{Tp})_2$ , along with predicted changes for each substitution (Figure S6), and the low-frequency ENDOR spectra of the series of compounds (Figure S7), and the temperature-dependence of the NMR spectra of  $\text{Co}(\text{Tp})_2$  (Figure S8) are also provided, along with a derivation of eq 1 (PDF). This material is available free of charge via the Internet at <http://pubs.acs.org>.

IC800245K